

# Modeling and design of Galfenol unimorph energy harvesters

Zhangxian Deng and Marcelo J Dapino

Smart Vehicle Concepts Center, Department of Mechanical and Aerospace Engineering, The Ohio State University, Columbus, OH 43210, USA

E-mail: [dapino.1@osu.edu](mailto:dapino.1@osu.edu)

Received 31 January 2015, revised 12 August 2015

Accepted for publication 2 October 2015

Published 5 November 2015



## Abstract

This article investigates the modeling and design of vibration energy harvesters that utilize iron-gallium (Galfenol) as a magnetoelastic transducer. Galfenol unimorphs are of particular interest; however, advanced models and design tools are lacking for these devices. Experimental measurements are presented for various unimorph beam geometries. A maximum average power density of  $24.4 \text{ mW cm}^{-3}$  and peak power density of  $63.6 \text{ mW cm}^{-3}$  are observed. A modeling framework with fully coupled magnetoelastic dynamics, formulated as a 2D finite element model, and lumped-parameter electrical dynamics is presented and validated. A comprehensive parametric study considering pickup coil dimensions, beam thickness ratio, tip mass, bias magnet location, and remanent flux density (supplied by bias magnets) is developed for a 200 Hz,  $9.8 \text{ m s}^{-2}$  amplitude harmonic base excitation. For the set of optimal parameters, the maximum average power density and peak power density computed by the model are 28.1 and  $97.6 \text{ mW cm}^{-3}$ , respectively.

Keywords: Galfenol, unimorph, energy harvesting

(Some figures may appear in colour only in the online journal)

## 1. Introduction

Iron-gallium Galfenol alloys exhibit moderate magnetostriction (around 400 ppm) and magnetization (around  $1200 \text{ kA m}^{-1}$  [1]). Unlike brittle Terfenol-D and piezoelectric materials, Galfenol has a high mechanical tensile strength (500 MPa) [2] while being able to support shear and shock loads. Being an iron-based alloy, Galfenol can be machined, welded, and formed. Further, Galfenol maintains significant magnetomechanical coupling over a broad temperature range [3, 4], making it attractive for practical actuators, sensors, and energy harvesters.

Vibration energy harvesters convert vibratory energy into electrical energy for purposes of supplying wireless sensors and other low-power embedded devices. Because they scavenge energy that would otherwise be lost, they can reduce battery requirements and thus reduce cost, complexity, and mass. Vibration energy harvesters have been successfully implemented using passive materials. Meninger *et al* [5]

developed an electrostatic harvester that operate as a variable capacitor to convert mechanical kinetic energy to electrical energy. Glynne-Jones *et al* [6] designed and optimized an electromagnetic harvester based on moving magnets inside of a static coil. Xing *et al* [7] presented a passive cantilever beam based on a high magnetic permeability material that generated a power density of  $1.07 \text{ mW cm}^{-3}$ .

Compared with traditional passive energy harvesters, smart materials including piezoelectric and magnetostrictive materials can exhibit higher energy conversion characteristics while utilizing no moving parts. This characteristic can help reduce system mass and bulk. Beeby *et al* [8] reviewed several existing piezoelectric generators for microsystem applications and showed that the maximum power density of these devices is about  $0.37 \text{ mW cm}^{-3}$  [9]. Piezomagnetoelastic energy harvesters were shown to yield an output power density of  $13 \text{ mW cm}^{-3}$  [10]. Wang and Yuan [11] implemented a Metglas beam as a vibratory energy harvester and obtained an output power density of  $0.9 \text{ mW cm}^{-3}$ . Berbyuk

**Table 1.** Comparison of mechanical vibration harvesters.

| Source                    | Description                   | Excitation frequency (Hz) | Excitation acceleration (m s <sup>-2</sup> ) | Power density (mW cm <sup>-3</sup> ) |
|---------------------------|-------------------------------|---------------------------|--|--------------------------------------|
| Roundy <i>et al</i> [9]   | Brass/PZT/Tungsten cantilever | 120                       | 2.5  | 0.37                                 |
| Erturk <i>et al</i> [10]  | Piezoelectric unimorph        | 8                         | 4.9  | 13                                   |
| Wang and Yuan [11]        | Metglas cantilever            | 58.1                      | 8.06   | 0.9                                  |
| Yoo <i>et al</i> [13, 14] | Galfenol unimorph             | 222                       | 9.8  | 3.84                                 |

[12] presented a Galfenol harvester which converts axial vibration energy to electrical energy, achieving a power density of 338 mW cm<sup>-3</sup>. Yoo and Flatau [13, 14] developed a unimorph energy harvester and validated it over a range of temperatures. Ueno and Yamada [15] proposed a bimorph Galfenol harvester that generated a maximum peak power density of 200 mW cm<sup>-3</sup>. Typical piezoelectric and magnetostrictive vibration harvesters presented in the literature are compared in table 1. Magnetostrictive energy harvesters can achieve moderate to high power density without suffering from depolarization issues. They also have a favorably low output impedance.

The lack of accurate and computationally efficient device models hinders the development of magnetostrictive harvester designs. Yoo and Flatau [13] simplified their unimorph device into a spring-damper-mass model but the model significantly over predicts the pickup coil voltage output. Wang and Yuan [11] developed a magnetostrictive beam model based on continuous vibration theory, but they utilized a linearized material model that also over predicts the output. A finite element analysis (FEA) model proposed by Chakrabarti and Dapino [16] and a subsequent model by Deng and Dapino [17] accurately describe the dynamic nonlinear response of Galfenol but they are not efficient enough to be implemented in model-guided design. Rezaeealam *et al* [18] implemented Armstrong's model to generate interpolation functions and presented a static 3D FEA model built in COMSOL Multiphysics for Galfenol-based bimorph harvesters. Accurate flux density calculations were presented, but no parametric studies were proposed.

In this study, a simplified 2D FEA model is first developed in COMSOL Multiphysics to describe the mechanical and magnetic response of Galfenol unimorph harvesters. Electrical dynamics from the pickup coil and a resistive load are represented by a lumped parameter model which takes the output from the FEA model as input. Five unimorph harvesters with different thickness ratios and tip masses are tested to validate the proposed model. Load matching analysis is performed to quantify the inductance of the pickup coil and to experimentally quantify the power output of the unimorph harvester. Finally, a parametric study considering coil size, beam thickness ratio, tip mass, and the remanent flux density of bias magnets is presented to maximize average and peak power densities.

## 2. Theory

### 2.1. Discrete energy averaged (EA) model

Constitutive Galfenol models for calculation of strain and magnetization have been proposed by Armstrong [19], Restorff *et al* [2], and Evans and Dapino [20], among others. In the latter, the number of easy directions was reduced to only six, yielding an EA model for cubic symmetric Galfenol based on local energies calculated in the vicinity of the easy directions. The local Gibbs energy in the EA model is defined as

$$G^k = \frac{1}{2} K^k |\mathbf{m}^k - \mathbf{c}^k|^2 - \mathbf{S}_m^k \cdot \mathbf{T} - \mu_0 M_s \mathbf{m}^k \cdot \mathbf{H}, \quad (1)$$

where  $k$  is an index that represents each easy direction,  $K^k$  is the anisotropy constant,  $\mathbf{m}^k$  is the moment orientation,  $\mathbf{c}^k$  is the easy direction,  $\mathbf{S}_m^k$  is the magnetostriction,  $\mathbf{T}$  is the stress tensor, and  $\mathbf{H}$  is the magnetic field vector.

The orientations of Galfenol moments are calculated through minimization of (1). Assuming  $|\mathbf{m}^k| \approx \mathbf{m}^k \cdot \mathbf{c}^k = 1$ , the analytical solution for moment orientations  $\mathbf{m}^k$  can be written as

$$\mathbf{m}^k = (\mathbf{K}^k)^{-1} \left[ \mathbf{B}^k + \frac{1 - \mathbf{c}^k \cdot (\mathbf{K}^k)^{-1} \mathbf{B}^k}{\mathbf{c}^k \cdot (\mathbf{K}^k)^{-1} \mathbf{c}^k} \mathbf{c}^k \right], \quad (2)$$

where  $\lambda_{100}$  is the maximum magnetostriction,  $\lambda_{111}$  is the maximum shear magnetostriction,

$$\mathbf{K}^k = \begin{bmatrix} K^k - 3\lambda_{100}T_1 & -3\lambda_{111}T_4 & -3\lambda_{111}T_6 \\ -3\lambda_{111}T_4 & K^k - 3\lambda_{100}T_2 & -3\lambda_{111}T_5 \\ -3\lambda_{111}T_6 & -3\lambda_{111}T_5 & K^k - 3\lambda_{100}T_3 \end{bmatrix}, \quad (3)$$

and

$$\mathbf{B}^k = \left[ c_1^k K^k + \mu_0 M_s H_1 c_2^k K^k + \mu_0 M_s H_2 c_3^k K^k + \mu_0 M_s H_3 \right]^T. \quad (4)$$

The bulk magnetization  $\mathbf{M}$  and magnetostriction  $\mathbf{S}_m$  are the weighted sum of the magnetization  $M_s \mathbf{m}^k$  and magnetostriction  $\mathbf{S}_m^k$  due to each orientation

$$\mathbf{M} = M_s \sum_{k=1}^6 c^k \mathbf{m}^k, \quad \mathbf{S}_m = \sum_{k=1}^6 c^k \mathbf{S}_m^k, \quad (5)$$

**Table 2.** Galfenol material properties used in this study.

| $K_{100}$ (kJ m <sup>-3</sup> ) | $\lambda_{100}$ (ppm) | $\lambda_{111}$ (ppm) | $\Omega$ (J m <sup>-3</sup> ) | $E_s$ (GPa) | $\mu_0 M_s$ (T) |
|---------------------------------|-----------------------|-----------------------|-------------------------------|-------------|-----------------|
| 30                              | $2/3 \times 280$      | $-20/3$               | 1200                          | 60          | 1.6             |

where  $\xi^k$  is the weight or volume fraction of the  $k$ th orientation. The magnetostriction of a crystal with cubic symmetry can be written as [21]

$$\mathbf{S}_m^k = \begin{bmatrix} (3/2)\lambda_{100}(m_1^k)^2 \\ (3/2)\lambda_{100}(m_2^k)^2 \\ (3/2)\lambda_{100}(m_3^k)^2 \\ 3\lambda_{111}m_1^k m_2^k \\ 3\lambda_{111}m_3^k m_2^k \\ 3\lambda_{111}m_1^k m_3^k \end{bmatrix}, \quad (6)$$

where  $\mathbf{m}^k = [m_1^k, m_2^k, m_3^k]$ . The volume fraction  $\xi^k$  of each orientation is calculated through a Boltzmann-type, energy weighting expression:

$$\xi^k = \frac{e^{-G^k/\Omega}}{\sum_{k=1}^6 e^{-G^k/\Omega}}, \quad (7)$$

where  $\Omega$  is the Armstrong smoothing factor [19].

This study implements the EA model to generate interpolation functions for COMSOL Multiphysics v4.3b. The Galfenol material used in this study is rolled and heat treated as provided by Etrema Products, Inc., with the material properties listed in table 2. These material property values have proven accurate in previous research [16, 22, 23].

## 2.2. Rayleigh damping

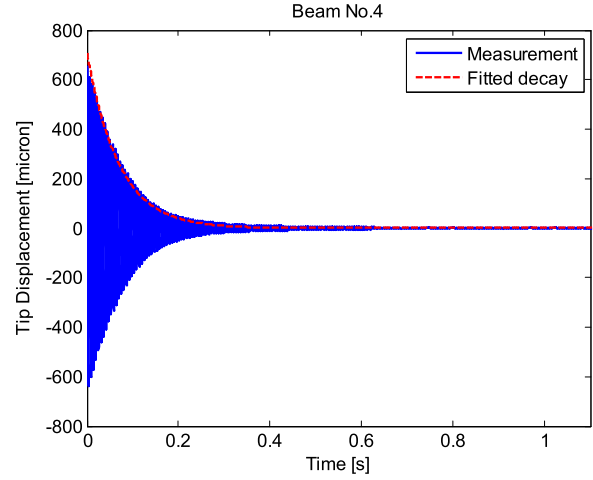
The structural damping is modeled as Rayleigh damping such that the damping matrix  $\mathbf{C}$  is formed by a linear combination of the mass matrix  $\mathbf{M}$  and stiffness matrix  $\mathbf{K}$  [24],

$$\mathbf{C} = \alpha\mathbf{M} + \beta\mathbf{K}. \quad (8)$$

Rayleigh damping coefficients  $\alpha$  and  $\beta$  can be evaluated from  $\xi_m$  and  $\xi_n$ , which denote the damping ratios associated with the specific natural frequencies  $\omega_m$  and  $\omega_n$  [25]:

$$\begin{bmatrix} \alpha \\ \beta \end{bmatrix} = \frac{2\omega_m\omega_n}{\omega_m^2 - \omega_n^2} \begin{bmatrix} \omega_n & -\omega_m \\ -1/\omega_n & 1/\omega_m \end{bmatrix} \begin{bmatrix} \xi_m \\ \xi_n \end{bmatrix}. \quad (9)$$

The impulse response of a unimorph beam with a thickness ratio of 2 is shown in figure 1. The decay curve best fits the measurement for a damping ratio of 0.0076. The natural frequency (244 Hz) can be obtained from the power spectrum of the impulse response. Assuming that the damping ratio is the same for the natural frequency and the second harmonic,  $\alpha$  and  $\beta$  can be directly calculated [23]. Type 316 stainless steel with a modulus of around 200 GPa is selected as the substrate material in this study. Epoxy glue Bond-200 (Vishay Intertechnology Inc.) is used to bond the Galfenol

**Figure 1.** Impulse response of the Galfenol unimorph beam with a thickness ratio of 2.**Table 3.** Beam geometries and damping ratios.

| Beam No.        | 1      | 2      | 3      | 4     | 5     |
|-----------------|--------|--------|--------|-------|-------|
| Thickness ratio | 1/3    | 2/3    | 4/3    | 2     | 3     |
| Damping ratio   | 0.0076 | 0.0078 | 0.0127 | 0.006 | 0.012 |
| Tip mass (g)    | 3.22   | 3.22   | 3.62   | 3.78  | 3.78  |

layer and the substrate layer. Table 3 shows the damping ratio, thickness ratio and tip masses of 5 different unimorph beams used in this study. The damping ratio of each unimorph is different due to variations in the glue layer thickness.

## 2.3. 2D COMSOL Multiphysics model, direct base excitation

**2.3.1. Uniaxial magnetization and magnetostriction.** A 3D fully nonlinear anhysteretic FEA model [16, 17] for the unimorph harvester shown in figure 2 is first implemented to investigate whether or not a simplified 2D FE model is sufficiently accurate. The thickness ratio of the unimorph beam, defined as the thickness of the substrate layer over the thickness of the Galfenol layer, is set to 1. The remanent flux density of the tip magnet is 1.8 T. Figures 3 and 4 are a sliced-view of the quasi-static flux density and magnetostriction through the center of the Galfenol layer in the  $x$ - $y$  plane. Compared with the flux density  $B_x$  along the length ( $x$ -axis) (figure 3(a)), the flux density  $B_y$  along the width ( $y$ -axis) (figure 3(b)) is negligible except near the magnet's end. Figure 3(a) also demonstrates that the variation of  $B_x$  along the width is insignificant excluding the region close to the edges. The same characteristics are observed in the magnetostriction calculations. Figure 4 shows that the

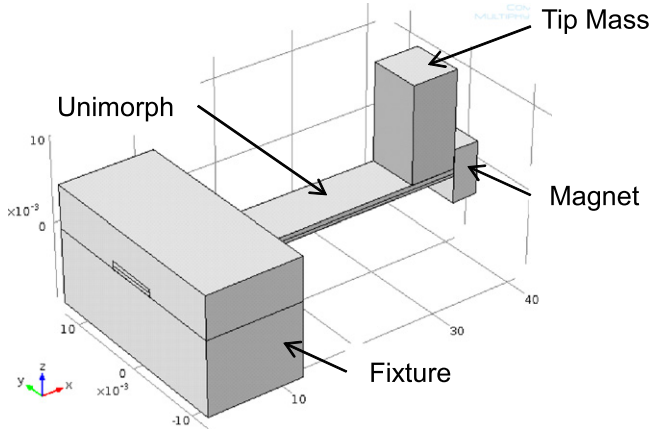


**Figure 2.** Geometry of 3D unimorph beam harvester as implemented in COMSOL Multiphysics.

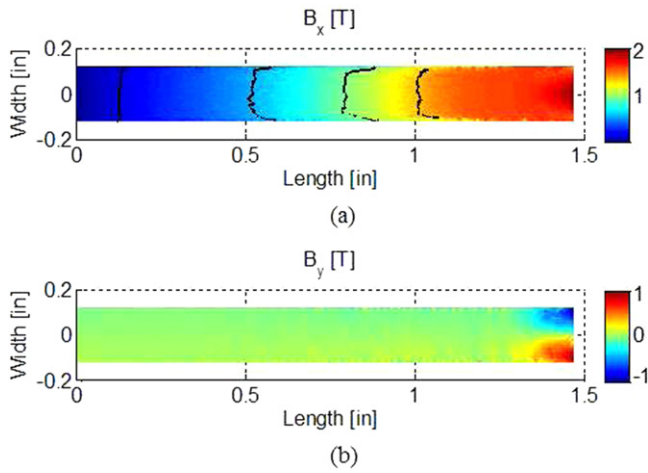


**Figure 3.** Flux density calculations: (a)  $B_x$ : flux density along the length of the Galferol layer (contours denote flux density levels of 0.2 to 1.4 T in 0.4 T steps); (b)  $B_y$ : flux density along the width.

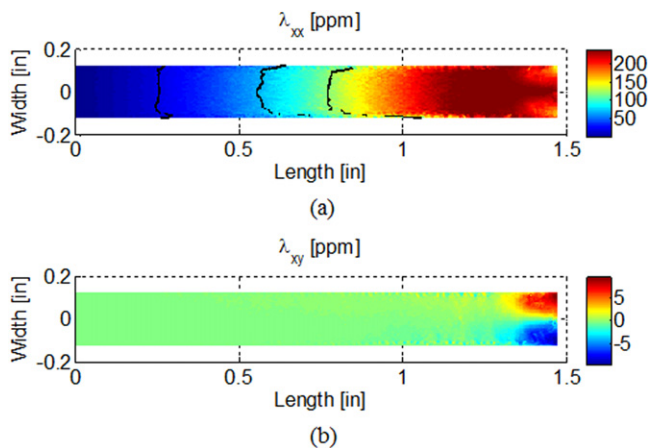


**Figure 4.** Magnetostriction calculations: (a)  $\lambda_{xx}$ : magnetostriction along the length of the Galferol layer (contours denote magnetostriction levels of 20 to 120 ppm in 50 ppm steps); (b)  $\lambda_{xy}$ : shear magnetostriction.

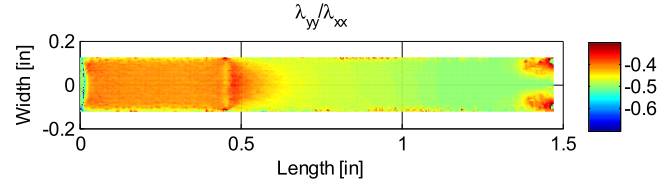


**Figure 5.** Transverse magnetostriction over longitudinal magnetostriction.

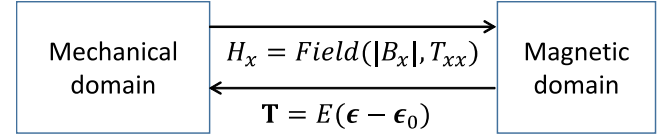


**Figure 6.** Full magnetomechanical coupling using lookup tables.

magnetostriction  $\lambda_{xx}$  along the  $x$ -axis is homogeneous along the  $y$ -axis, thus and a 2D model in the  $x$ - $z$  plane is a reasonable simplification for both magnetic and mechanical domains. The 2D model is 97% faster than the 3D model presented in [17].

### 2.3.2. Nonlinear magnetomechanical coupling lookup tables.

In addition to a decreased dimensionality and associated reduction in degrees of freedom, the speed advantage of this approach stems from the use of lookup tables calculated from the discrete EA model. No model inversion algorithms need to be called.

The nonlinear field-flux density ( $H$ - $B$ ) relationship of the Galferol layer is described using an interpolation function  $Field(B_x, T_{xx})$  in COMSOL Multiphysics v4.3b, where  $B_x$  is the flux density along the length and  $T_{xx}$  is the tensile stress along the length. Magnetostriction  $\lambda$  is modeled as an initial strain acting on the Galferol domain, starting with the relationship

$$\mathbf{T} = E(\boldsymbol{\epsilon} - \boldsymbol{\epsilon}_0), \quad (10)$$

in which  $\mathbf{T}$  is the stress tensor,  $E$  is the passive Young's modulus of the material,  $\boldsymbol{\epsilon}$  is the strain tensor and  $\boldsymbol{\epsilon}_0$  is the initial strain tensor

$$\boldsymbol{\epsilon}_0 = \begin{bmatrix} \lambda & 0 & 0 \\ 0 & -\lambda/2 & 0 \\ 0 & 0 & -\lambda/2 \end{bmatrix}. \quad (11)$$

To guarantee the volume consistency of the material, the initial strain in the  $y$  and  $z$  directions induced by  $\lambda_{xx}$  are defined as  $-\lambda/2$ . Figure 5 shows that  $\lambda_{yy}/\lambda_{xx}$  is around  $-0.5$  except near the magnet's end and inside the fixture. In this study, magnetostriction  $\lambda$  is also defined as an interpolation function  $\lambda(B_x, T_{xx})$ .

Figure 6 illustrates the two-way coupling between magnetic and mechanical domains in COMSOL Multiphysics. The stress-dependent magnetization or magnetic permeability is described by  $Field(B_x, T_{xx})$  and the field-dependent strain or Young's modulus is described by assuming an initial strain  $\boldsymbol{\epsilon}_0$  which is calculated from

$\lambda(B_x, T_{xx})$ . The built-in solver in COMSOL Multiphysics is able to find the converged solutions of  $T_{xx}$  and  $H_x$  through iterations.

#### 2.4. 2D COMSOL multiphysics model, indirect tip excitation

The fully coupled finite element model based on lookup tables as shown in figure 6 is appropriate for any magnetostrictive system as long as the magnetization and magnetostriction are uniaxial. Because the damping ratio of the unimorph beam is small, most of the simulation time would be spent on computing the transient state (30–40 excitation cycles) if dynamic base excitation was directly applied. To eliminate the time consuming transient simulation, a two-step analysis is presented.

**2.4.1. Two-step analysis for base excitations.** The simulation in this study is divided into two steps. In the first step, the Galfenol layer is considered as a passive material with constant modulus. According to experimental results on unimorph resonance frequencies, the equivalent Young's modulus of Galfenol is  $E_G \approx 54$  GPa. The COMSOL Multiphysics eigenfrequency solver is implemented to obtain both natural frequencies and tip displacement amplitudes. In the second step, the calculated tip displacement is assumed to be a sinusoidal function and applied as a boundary condition to the fully coupled 2D Galfenol model. Through the above simplifications, magnetic field dynamics and Galfenol hysteresis are ignored. The unimorph beam model reaches steady state after only 2 cycles. The two-step analysis is valid only if the Delta-E effect in the Galfenol layer is not significant. However,  $E_G$  varies with respect to applied magnetic field and stress. The modeling error due to the Young's modulus change is quantified in the following paragraph.

For a passive cantilever beam with stiffness  $k_b$ , damping coefficient  $c_b$ , and effective mass  $m_b$ , the amplitude of tip deflection  $|D_{\text{tip}}(f)|$  with respect to base excitation frequency  $f$  is

$$|D_{\text{tip}}(f)| = \frac{A_0}{(2\pi f)^2} \sqrt{\frac{k_b^2 + (2\pi f c_b)^2}{[k_b - m_b(2\pi f)^2]^2 + (2\pi f c_b)^2}}, \quad (12)$$

where  $A_0$  is the amplitude of base acceleration. Assuming  $E_G = 54$  GPa (as an average), the tip deflection calculated from (12) is compared with experimental data in figure 7. The discrepancy between experiments and calculations is about 0.8%. Hence, the modulus variation in the Galfenol unimorph is negligible and the two-step approach is justified.

#### 2.5. Lumped-parameter model for electrical circuit dynamics.

Magnetostrictive harvesters require supporting electronic circuits for energy conversion and storage. Directly incorporating electrical dynamics into FE models dramatically slows down the computation and weakens the model convergence. Since this study is focused on model-based design, computational efficiency is necessary. For this reason, the

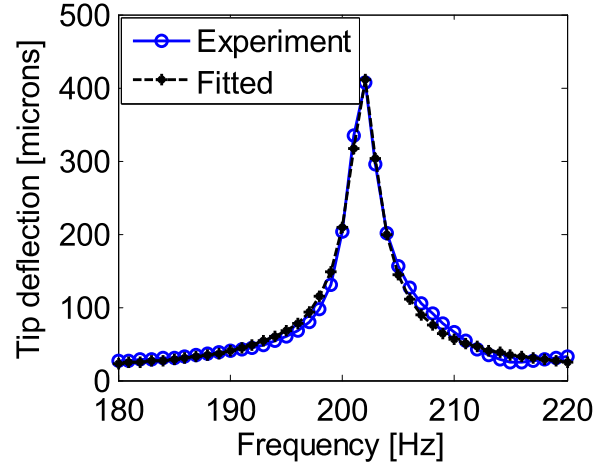


**Figure 7.** Tip deflection of the unimorph (thickness ratio of 2) with respect to  $9.8 \text{ m s}^{-2}$  amplitude and varying frequency base excitation: experimental results (solid) and modeling results calculated from (12) (dashed).

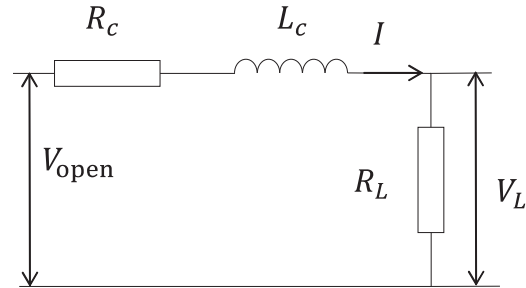


**Figure 8.** Equivalent electrical circuit for resistive load ( $R_c$ : pickup coil resistance,  $R_L$ : load resistance,  $L_c$ : pickup coil inductance.).

electrical dynamics are described with a lumped-parameter model.

The electrical domain is one-way coupled with the magnetic domain through Faraday's law of magnetic induction. This implies that magnetic field generation from induced currents (Ampere's law) is neglected. The full magnetoelastic coupling represented by figure 6 is described with the two aforementioned interpolation functions in COMSOL Multiphysics. The 2D FEA model is computed in quasi-static mode to evaluate the average flux density through the cross-section of the pickup coil. The input voltage  $V$  is calculated through Faraday's law

$$V_{\text{open}} = -NA \frac{dB}{dt}, \quad (13)$$

where  $NA = 150 \text{ cm}^2$  is the coil constant.

An equivalent electrical circuit, shown in figure 8, is set up to model the electrical dynamics of the pickup coil and the attached resistive load. The pickup coil inductance is estimated as

$$L_c = \frac{\mu_G \mu_0 N^2 A_G}{l}, \quad (14)$$

where  $A_G$  is the cross sectional area of the Galfenol layer,  $N$  is the number of turns,  $l$  is the length of the coil,  $\mu_0$  is the



permeability of free space, and  $\mu_G$  is the relative permeability of Galfenol which changes with respect to stress and magnetization. Since the permeability of Galfenol exhibits a relatively small variation in this study, an average permeability of 200 is assumed. The coil resistance is estimated as

$$R_c = \frac{\pi(r_1 + r_2)N}{\rho A_c}, \quad (15)$$

where  $r_1$  is the inner radius of the coil,  $r_2$  is the outer radius of the coil,  $\rho$  is the conductivity of the magnet wire, and  $A_c$  is the cross sectional area of the wire.

The effectiveness of a unimorph harvester is quantified by the average power  $\bar{P}$  consumed by the resistive load, the average power density  $\bar{D}$ , and the peak power density  $Dp$  as

$$\bar{P} = \frac{\int_0^t (V_L^2/R_L) dt}{t}, \quad \bar{D} = \frac{\bar{P}}{V_{\text{eff}}}, \quad Dp = \frac{V_{\text{amp}}^2}{R_L V_{\text{eff}}}, \quad (16)$$

where  $V_L$  is the voltage measured across the load,  $R_L$  is the resistance of the load,  $V_{\text{amp}}$  is the amplitude of  $V_L$ , and  $V_{\text{eff}}$  is the effective volume of the Galfenol layer (excluding the material within the fixture).

Several figures of merit have been utilized in the literature for vibration energy harvesters [27]. For a given vibration source, the power density  $\bar{D}$  is able to best describe energy harvesting performance. Hence,  $\bar{D}$  is used in the parametric study as the target function.

It is emphasized that the literature on magnetostrictive harvesters reveals many different ways to calculate power density, depending on what effective volume is used. No approach has been proven ideal so far, and no standards exist to calculate power density. We are following best practices found in the magnetostriction literature by considering the effective volume of the active layer. Other studies, like Xing *et al* [7] for passive cantilevers, considered the freespace enclosed by the vibrating beam. This approach has its own problems since the deflection of the beam depends on both the structure and the excitation, making it impossible to discern between the performance of the active material and that derived from the excitation source. For active harvesters, the volume of active material is a better alternative.

To maximize the output of a Galfenol unimorph harvester, load resistance  $R_L$  must be carefully selected. Because of the nonlinear behavior of Galfenol, the output voltage  $V_{\text{open}}$  harvested from the coil is not exactly a sinusoidal wave. However, the power spectrum of  $V_{\text{open}}$  shows that the fundamental frequency ( $\omega$ ) component contains most of the spectral energy (figure 9). Hence,  $R_L$  is selected under the assumption that  $V_{\text{open}}$  is a sinusoidal wave. The average output power dissipated by the resistor is

$$\begin{aligned} \bar{P} &= \frac{R_L}{(R_c + R_L)^2 + (\omega L_c)^2} \int_0^T V_{\text{open}}(t)^2 dt / T \\ &= \frac{|V_{\text{open}}|^2}{2} \frac{R_L}{(R_c + R_L)^2 + (\omega L_c)^2}, \end{aligned} \quad (17)$$

where  $T$  is the period of the voltage signal. The impedance matching principle dictates that the maximum average power

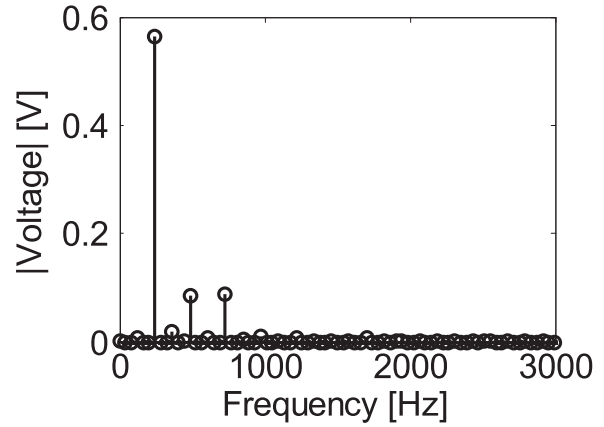


**Figure 9.** Fast Fourier transform (FFT) of the open-circuit voltage output by a unimorph harvester with a thickness ratio of 2.

$\bar{P}_{\text{max}}$  and the maximum average power density  $\bar{D}_{\text{max}}$  are achieved when  $R_L = \sqrt{R_c^2 + (\omega L_c)^2}$ , yielding

$$\bar{P}_{\text{max}} = \frac{V_{\text{amp}}^2}{4} \frac{1}{R_c + \sqrt{R_c^2 + (\omega L_c)^2}}, \quad (18)$$

$$\bar{D}_{\text{max}} = \bar{P}_{\text{max}} / V_{\text{eff}}. \quad (19)$$

The maximum peak power density  $Dp_{\text{max}}$  is

$$Dp_{\text{max}} = \frac{V_{\text{amp}}^2}{2\sqrt{R_c^2 + (\omega L_c)^2} + 2R_c} \frac{1}{V_{\text{eff}}}. \quad (20)$$

The above analysis is built on three major assumptions: (i) the fundamental frequency dominates over all of the harmonics; (ii) Ampere's law effects are negligible in the system; and (iii) the inductance of the pickup coil is constant. The modeling error introduced by each assumption is quantified in the following paragraphs.

**2.5.1. Dominance of fundamental frequency on the induced voltage.** Figure 9 shows the FFT of the measured open-circuit voltage generated by a harvester with a thickness ratio of 2. The fundamental frequency is about 243 Hz, which coincides with the base excitation frequency. The two harmonics observed arise from the nonlinearity of Galfenol. The transfer function describing the electrical circuit dynamics in figure 8 is

$$\frac{V_L}{V_{\text{open}}}(s) = \frac{R_L}{L_c s + (R_L + R_c)}. \quad (21)$$

The average output power harvested from the full voltage signal ( $\bar{P}_{\text{ori}}$ ) and from the fundamental frequency ( $\bar{P}_{\text{sine}}$ ) are

$$\bar{P}_{\text{ori}} = \frac{1}{T} \int_0^T \frac{V_{L,\text{ori}}^2}{R_L} dt, \quad \bar{P}_{\text{sine}} = \frac{1}{T} \int_0^T \frac{V_{L,\text{sine}}^2}{R_L} dt, \quad (22)$$

respectively. The terms  $V_{L,\text{ori}}$  and  $V_{L,\text{sine}}$  respectively denote the voltage across the resistive load considering the full signal and only the fundamental frequency. The relative error incurred in considering only the fundamental frequency is

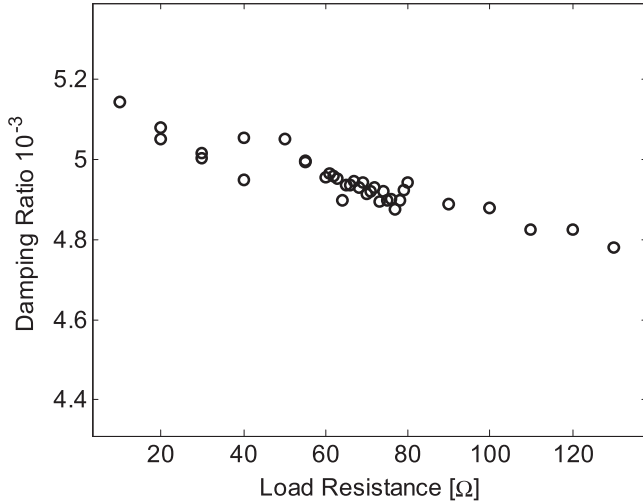


**Figure 10.** Damping ratio of the Galfenol unimorph with a thickness ratio of 2 and pickup coil length of 2.54 cm, for various resistive loads [28].

only  $E_0 = 2.8\%$ , where

$$E_0 = \frac{\bar{P}_{\text{ori}} - \bar{P}_{\text{sine}}}{\bar{P}_{\text{ori}}}. \quad (23)$$

Therefore, the assumption is valid.

**2.5.2. Negligible Ampere's law effects.** The flux variation in the Galfenol layer induces electric potential in the circuit via Faraday's law. Simultaneously, the induced current in the pickup coil produces a magnetic field along the length of the Galfenol element, which partially counteracts the bending of the unimorph. The effect of Ampere's law is equivalent to additional mechanical damping in the governing equations [26]. Figure 10 shows the damping ratio measured from a unimorph beam with a thickness ratio of 2 under various resistive loading conditions [28]. The damping ratio variation is about  $4 \times 10^{-4}$ , or 7.6%. From (12), the tip deflection at resonance is

$$D_{\text{tip}}(\omega_n) = \frac{A_0}{2\omega_n^2 \xi \sqrt{1 - \xi^2}}, \quad (24)$$

where  $\omega_n = \sqrt{k_b/m_b}$  is the resonance frequency of the beam. For  $\omega_n = 1256.6 \text{ rad s}^{-1}$  (200 Hz), the error associated with neglecting Ampere's law is, from (24), about 7.7%.

**2.5.3. Constant inductance of the pickup coil.** The magnetic permeability of Galfenol is stress- and field-dependent. The calculated average permeability in the Galfenol layer with respect to tip deflection is presented in figure 11. As the tip of the beam deflects downwards, the compressive stress forces magnetic domains in the Galfenol layer to rotate away from the beam's longitudinal direction, eventually saturating the material. When the displacement becomes positive, the tensile stress aligns magnetic moments along the beam's length and saturates the material as well. The permeability of Galfenol gradually approaches one at both saturation regions while it reaches a maximum for moderate compression (figure 11). A

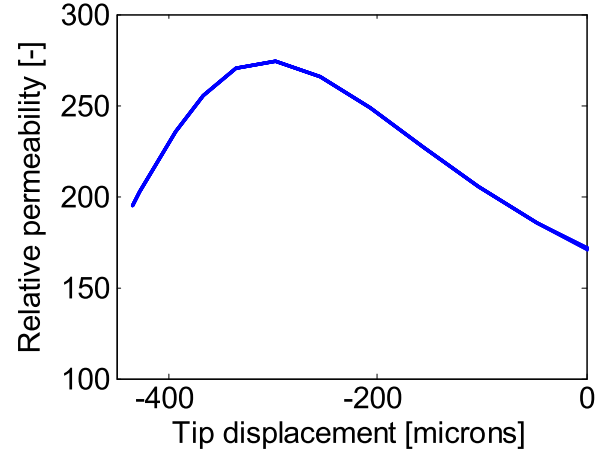


**Figure 11.** Average magnetic permeability in the Galfenol layer with respect to tip deflection for a Galfenol unimorph with a thickness ratio of 2.

reasonable permeability range can be selected as  $\mu_G = 200 \pm \delta\mu_G$ , where  $\delta\mu_G = 70$ , since the typical tip displacement of the unimorph beam observed in experiments is  $\pm 500$  microns. Substitution of (14) into (18) gives the average output power as

$$\bar{P}_{\text{max}} = \frac{V_{\text{amp}}^2}{4} \left[ R_c + \sqrt{R_c^2 + \left( \frac{\mu_G \mu_0 N^2 A_G \omega}{l} \right)^2} \right]^{-1}. \quad (25)$$

Assuming the coil resistance is  $47.4 \Omega$  (measured experimentally), the relative simulation error of the output power due to the constant permeability assumption is about 5.8% when the natural frequency is 200 Hz. The value of  $\delta\mu_G$  at high frequencies should be lower than 70 due to eddy currents and anomalous losses.

### 3. Experiments

#### 3.1. Setup

Yoo and Flatau [13] placed a Galfenol unimorph harvester directly on the surface of a shaker head. In that configuration, the magnetic field generated by the shaker's coil can disturb the Galfenol response. As shown in figure 12, an aluminum stage was employed in this study to separate the Galfenol beam from the magnetic field induced by the shaker's drive coil. The unimorph beam sits 11.176 cm (4.4 in.) above the shaker head, where the measured interference from the shaker's coil is negligible. All the components except the unimorph beam and magnets are made of either non-magnetic aluminum or brass to minimize their influence on the magnetic field. Further details are shown in figures 13 and 14.

#### 3.2. Model validation

The 2D FEA model for Galfenol-based unimorph beams is validated using measurements from the 5 unimorph beams listed in table 3. The amplitude of the base vibration is fixed at

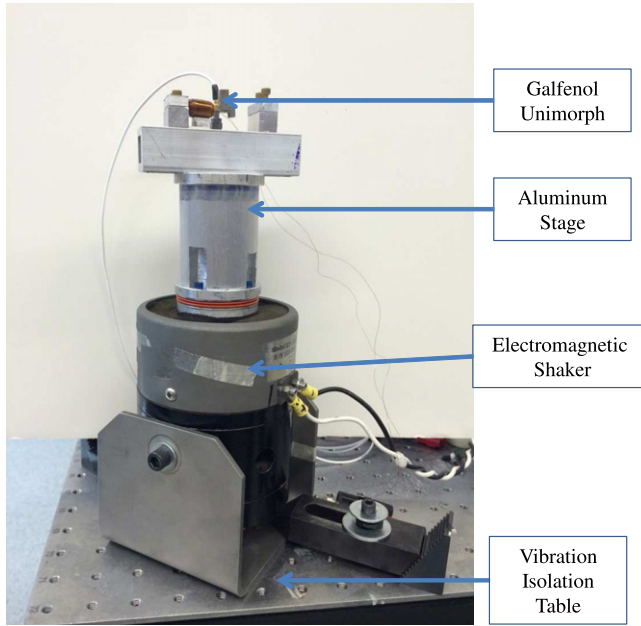


**Figure 12.** View of the shaker, mounting and isolation stages, and unimorph beam.

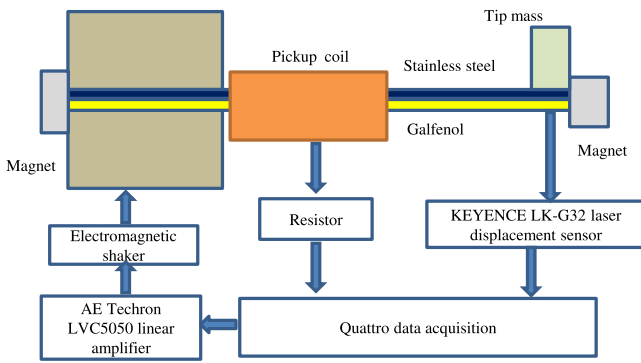


**Figure 13.** Experiment layout.

$9.8 \text{ m s}^{-2}$  throughout the experiments. Experimental measurements and model calculations are compared in figures 15 and 16. Figure 15 shows that the flux density through the cross-section of the pickup coil is adequately described. The voltage calculation is less accurate due to the derivative involved in relation (13). The flux density in the burst region is accurately simulated so the voltage amplitude is accurate.

Since the voltage in figures 15 and 16 is measured and simulated under open circuit conditions, the error investigated in section 2.5 will not influence the simulation. The modeling error is relatively large when the thickness ratio is small, which indicates two possible error sources: the tip deflection is larger in low thickness ratio beams, so that the assumptions discussed in sections 2.3 and 2.5 are less applicable; and part of the voltage on the coil was induced by movement of the magnets on the tip. Due to the former, a beam with a smaller thickness ratio has more voltage induced by the moving magnet. A moving mesh technique is able to take the latter into account.

In order to speed up computation, Deng and Dapino [29] proposed the two-step analysis through which the base excitation was converted to tip deflection. When this conversion is not applied, and the base excitation is directly applied to the 2D FEA model, the framework becomes more general and applicable to other magnetostrictive systems. Figure 16 compares the simulation results from direct base excitation inputs and from the two-step analysis. Both approaches provide similar accuracy. However, the two-step analysis took 3 min to generate 2 complete cycles of output voltage at steady state, while the computation time is about 2 h if base excitation is directly applied. The two-step approach is thus computationally efficient for model-guided design, without a compromise in accuracy.

### 3.3. Load matching

In the experiments, different resistive loads  $R_L$  are connected to the pickup coil. The geometry of the Galfenol layer is  $38.1 \text{ mm} \times 6.35 \text{ mm} \times 0.381 \text{ mm}$  (1.5 in.  $\times$  0.25 in.  $\times$  0.015 in.), but 11.43 mm (0.45 in.) of the Galfenol layer is clamped inside the fixture and does not generate flux variations. Further, the effective length is selected as 15.24 mm (0.6 in.) by only considering the section of Galfenol surrounded by the pickup coil.

The maximum values of  $\bar{P}$ ,  $\bar{D}$ , and  $Dp$  are observed from beam No. 4, as shown in figures 17 and 18, giving 0.9 mW,  $24.4 \text{ mW cm}^{-3}$ , and  $63.6 \text{ mW cm}^{-3}$ , respectively.

The pickup coil resistance has a value of  $36.8 \Omega$ . According to figure 17, the maximum value of  $\bar{P}$  is achieved when the load resistance  $R_L$  is slightly larger than the resistance of the pickup coil  $R_c$ , due to the inductance of the coil  $L_c$ .

It was shown that the 2D finite element unimorph beam model is accurate for this particular harvester design,

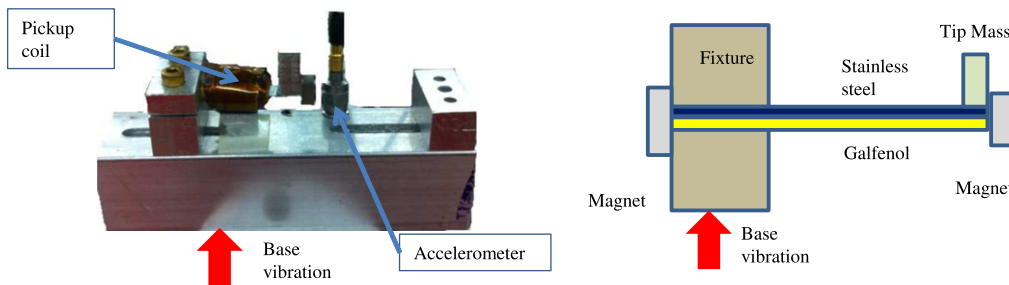


**Figure 14.** Cantilever Galfenol unimorph harvester.



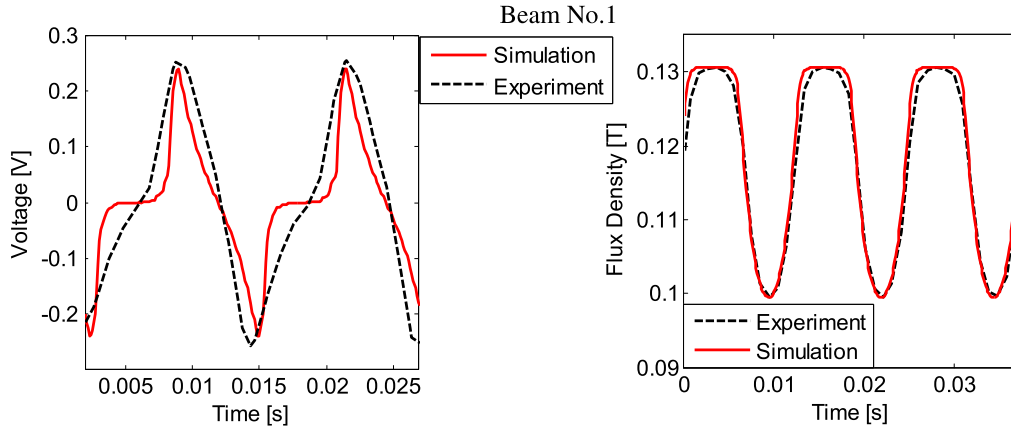


**Figure 15.** Pickup coil voltage and flux density through the cross-section of the pickup coil for beam No. 1.

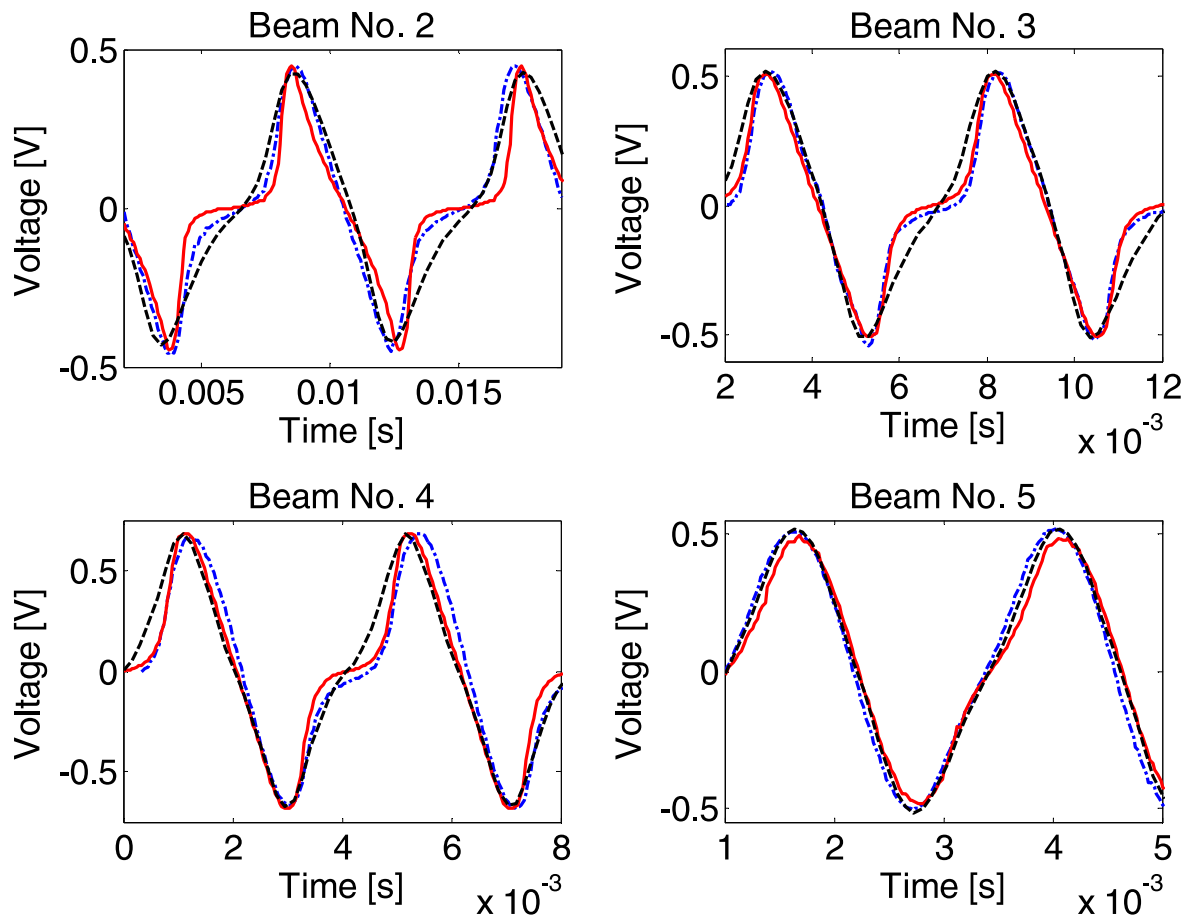


**Figure 16.** Pickup coil voltage for beams No. 2–5. Blue dotted lines: modeling results by applying base excitation directly. Red solid lines: modeling results by converting base excitation to tip excitation. Black dashed lines: experimental results.

where the magnetic flux and the magnetostriction are oriented along the unimorph length direction. The model can thus be used as a tool to optimize future unimorph harvesters. Deng and Dapino [29] implemented the proposed finite element method to optimize individual design parameters including pickup coil size, beam thickness ratio, and bias magnetic field strength. However, parameter effects are coupled, thus this study offers a comprehensive, fully

coupled parametric study considering pickup coil size, beam thickness ratio, tip mass, and bias magnet strength for a 200 Hz,  $9.8 \text{ m s}^{-2}$  harmonic base excitation. Both experimental and modeling results show that placing the bias magnet on the fixture produces higher power density than placing it on the beam tip. Hence, this parametric study only considers the unimorph beam setup shown in figure 19.

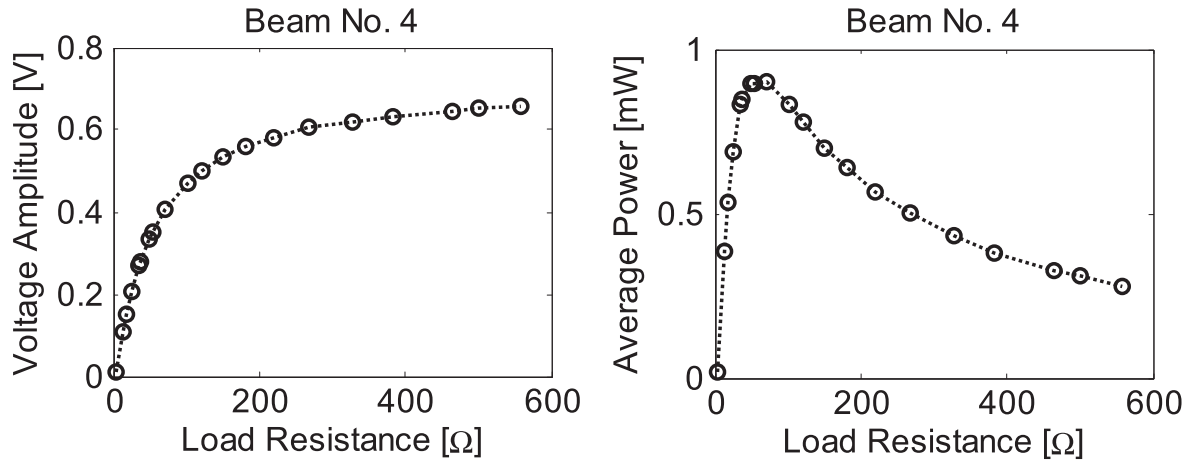


Figure 17. Output voltage (left) and average output power (right) versus load resistance for beam No. 4.

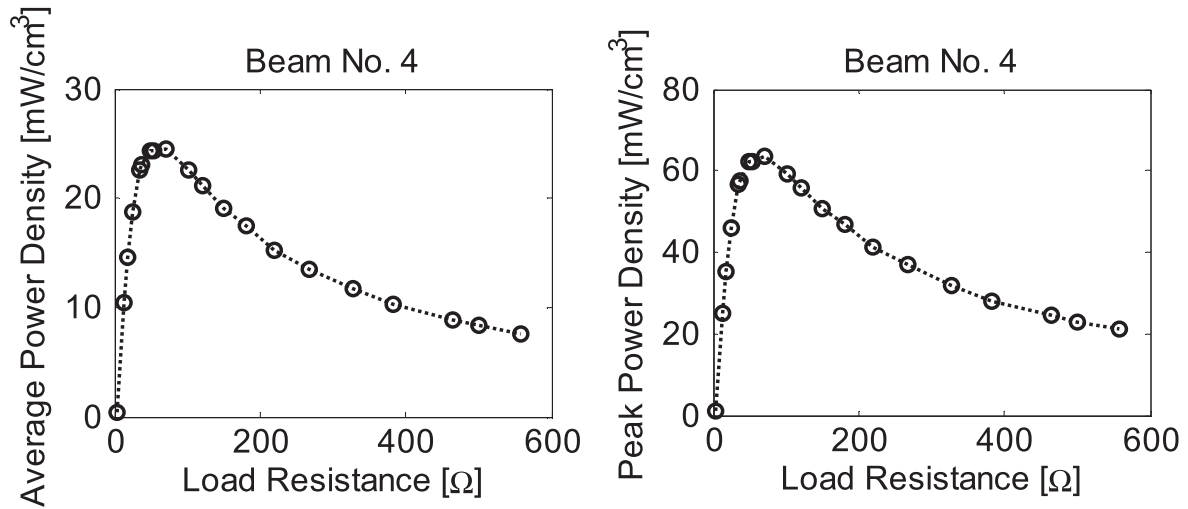


Figure 18. Average power density (left) and peak power density (right) versus load resistance for beam No. 4.

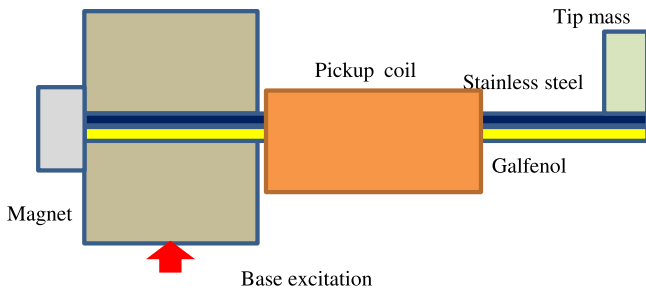


Figure 19. Unimorph harvester geometry used in the parametric study.

### 3.4. Pickup coil size

The voltage scavenged from the bending unimorph beam increases monotonically with pickup coil size. However, the outer layers of the coil become insensitive to the flux change through the Galfenol layer coil size increases. On the other hand, the resistance of the coil also increases with coil size, which limits the coil's output power. Hence, optimal parameters for the pickup coil should be found.

In this study, the wire gauge size of the pickup coil is 36 (American Wire Gauge) and the length of the pickup coil is fixed to 15.24 mm (0.6 in.). The number of turns per layer is 40 and the thickness per layer is 0.213 mm (0.0084 in.). To guarantee the unimorph beam not touching the coil during bending, the inner layer of the coil is 0.762 mm (0.03 in.) away from the beam surface. Assuming that the electrical load is resistive and load resistance  $R_L = \sqrt{R_c^2 + (2\pi f)^2 L_c^2}$ , where the coil resistance  $R_c$  and coil inductance  $L_c$  are calculated in COMSOL Multiphysics, the only parameter that needs to be studied is the number of turns of the pickup coil.

The pickup coil is optimized alone using a 3D geometry (figure 20(a)) where bending of the unimorph beam is neglected and the average flux density variation through the Galfenol layer  $B_x$  is assumed to follow a 200 Hz sinusoidal wave. In practice, the amplitude  $|B_x|$  varies with load. Figure 20(b) shows that the optimal number of turns (800 turns in this case) is independent from  $|B_x|$ . Thus the pickup coil can be optimized separately without incurring in substantial error.

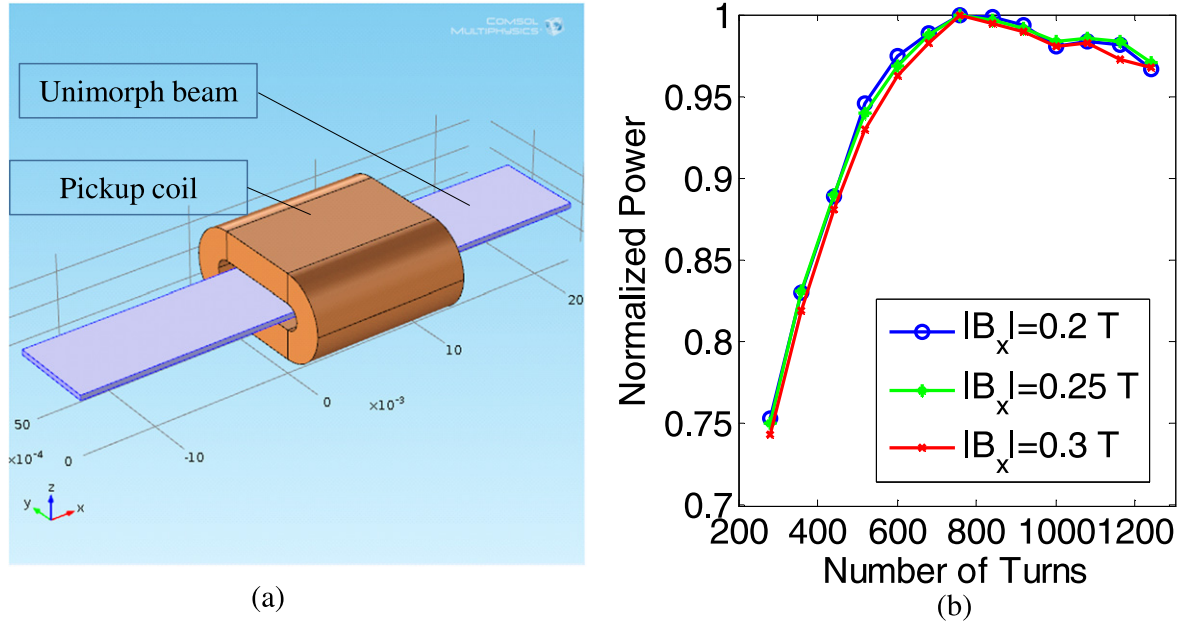


**Figure 20.** Left: 3D geometry in COMSOL Multiphysics for pickup coil optimization. Right: normalized average output power with respect to number of turns under different  $|B_x|$  values.

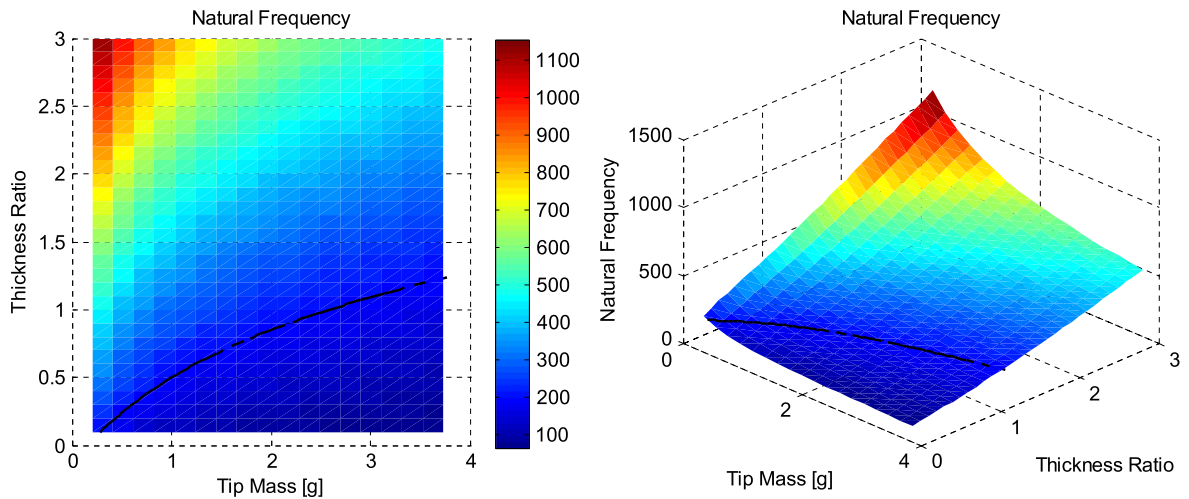


**Figure 21.** Natural frequency of the unimorph beam with respect to tip mass and thickness ratio. Black line: natural frequency equal to 200 Hz.

### 3.5. Thickness ratio and tip mass

To achieve a unimorph beam with a natural frequency of 200 Hz, both tip mass and beam thickness ratio must be selected. Since the Galfenol layer operates at relative high frequency and the tensile stress induced by bending is not enough to drive the material over the whole burst region, the modulus variation (Delta-E effect) of the Galfenol layer is negligible. This study assumes an average modulus of 54 GPa for the Galfenol layer. After placing a constraint on the size of the tip mass, the maximum tip mass value is 3.7 g when brass is used. Figure 21 shows the calculated natural frequency with respect to tip mass and beam thickness ratio, with the black solid line showing the combination of tip mass and beam thickness ratio that produces a 200 Hz natural frequency. This

line is numerically fitted by the following polynomial function:

$$m_{\text{tip}} = -0.2141T_R^5 + 0.5638T_R^4 + 0.264T_R^3 + 0.4799T_R^2 + 1.3511T_R + 0.1438, \quad (26)$$

where  $T_R$  is the thickness ratio and  $m_{\text{tip}}$  is the weight of tip mass.

### 3.6. Bias magnet location

The purpose of placing permanent magnets near the unimorph beam is to create a suitable bias magnetic field in the Galfenol layer so that the material operates close to its burst region, where the magnetoelastic coupling is most

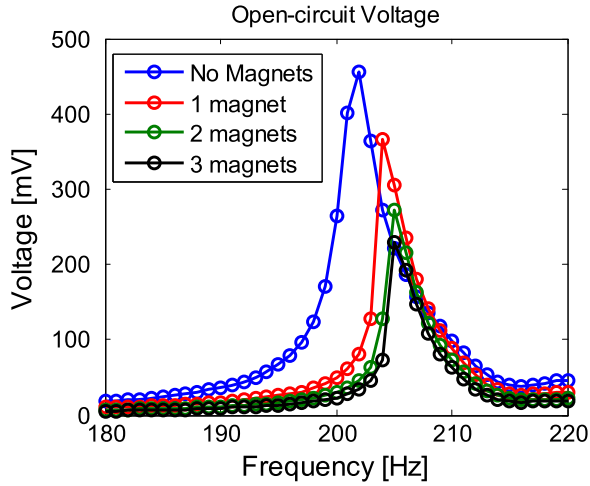


**Figure 22.** Open-circuit voltage versus number of magnets in the fixture when a single magnet is placed near the tip of the beam.

significant. In this study, the following configurations of bias magnets were investigated: magnets near the tip of the beam, magnets in the fixture, and magnets in both the fixture and near the beam's tip. Comparison between the first and third configurations was performed experimentally. Figure 22 shows the amplitude of output voltage (fundamental frequency only) versus excitation frequency when different numbers of magnets were added to the fixture. As the number of magnets in the fixture increases, the natural frequency of the beam increases due to the Delta-E effect. Placing magnets at both ends will saturate the Galferol element, making it stiffer, and produce relatively low output voltage. Hence, the first configuration is better than the third one.

Comparison between the first and second configurations was not conducted experimentally since removing the tip magnet changes the natural frequency of the harvester. The location of the material's burst region depends on both stress and magnetic field strength, and a larger magnetic field is required to reach the burst region at a higher compressive stress [30]. The tip mass and initial magnetostriction of

Galferol creates pre-compression in the Galferol layer. Euler–Bernoulli beam theory indicates that this pre-compressive stress decreases from the unimorph's base to its tip. Hence a similar decreasing magnetic field from the base to the tip is preferred. The second configuration, shown in figure 19, can easily achieve such a magnetic field and is thus better than the first configuration.

### 3.7. Bias magnet strength

The remanent flux density of the tip bias magnet  $B_r$  is optimized for beam thickness ratios varying from 0.3 to 1.3. The tip mass is selected according to (26) so that a 200 Hz natural frequency is achieved. Limited by the size of permanent magnets used in this study, the commercially available  $B_r$  value ranges from 0.1 to 1.8 T. The output is evaluated using (19) and (20). Based on the pickup coil size selected from section 3.4, the resistance of the coil  $R_c = 47.4 \Omega$  which is calculated from (15). The coil inductance  $L_c = 25.5$  mH is estimated from (14). This parametric study step assumes  $R_L = \sqrt{R_c^2 + (\omega L_c)^2}$ .

Figures 23 and 24 present the maximum average output power  $\bar{P}_{\max}$  and the maximum average output power density  $\bar{D}_{\max}$  with respect to different thickness ratios and bias magnet strengths. Since  $\bar{P}_{\max}/\bar{D}_{\max} = V_{\text{eff}}$  which is constant, modeling results of both parameters follow the same trend. The  $\bar{P}_{\max}$  first increases and then decreases along the bias magnet strength  $B_r$  direction, because the bias magnetic field first drives the material to the burst region and then saturates the material as the magnetic field continues to increase. Along the thickness ratio axis,  $\bar{P}_{\max}$  increases monotonically, since a thicker passive layer pushes the Galferol layer further away from the beam's mid-plane and induces higher stress variation in Galferol. The peaks in figures 23 and 24 ( $\bar{P}_{\max} = 1.0$  mW and  $\bar{D}_{\max} = 28.1$  mW cm<sup>-3</sup>) are located at the position where the thickness ratio is 1.3 and  $B_r = 1.4$  T.

Figure 25 presents the maximum peak output power density  $Dp_{\max}$ . It has a trend which is similar to figures 23 and

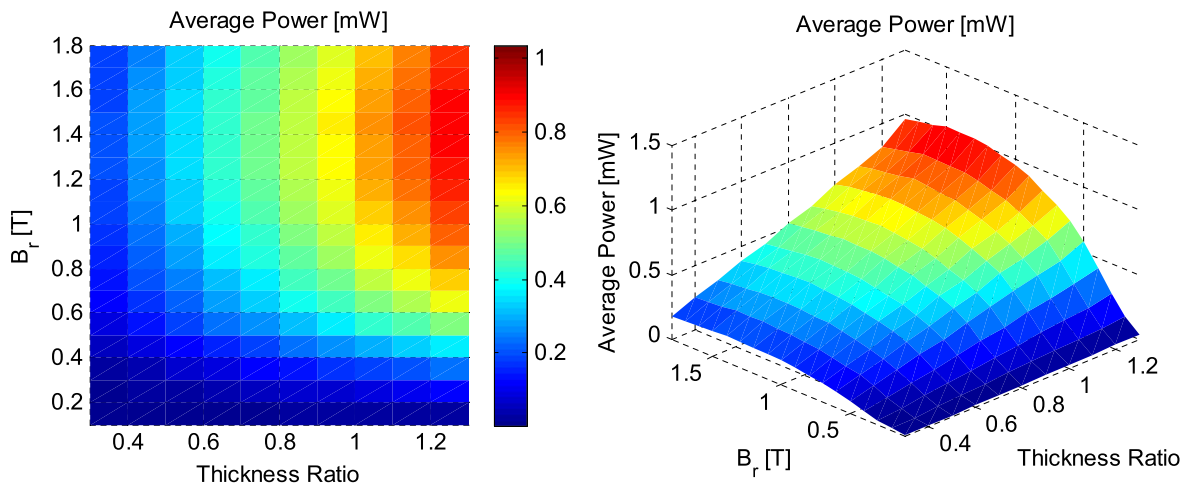


**Figure 23.** Maximum average output power  $\bar{P}_{\max}$  with respect to thickness ratio and bias magnetic strength for 200 Hz,  $9.8 \text{ m s}^{-2}$  base excitation.

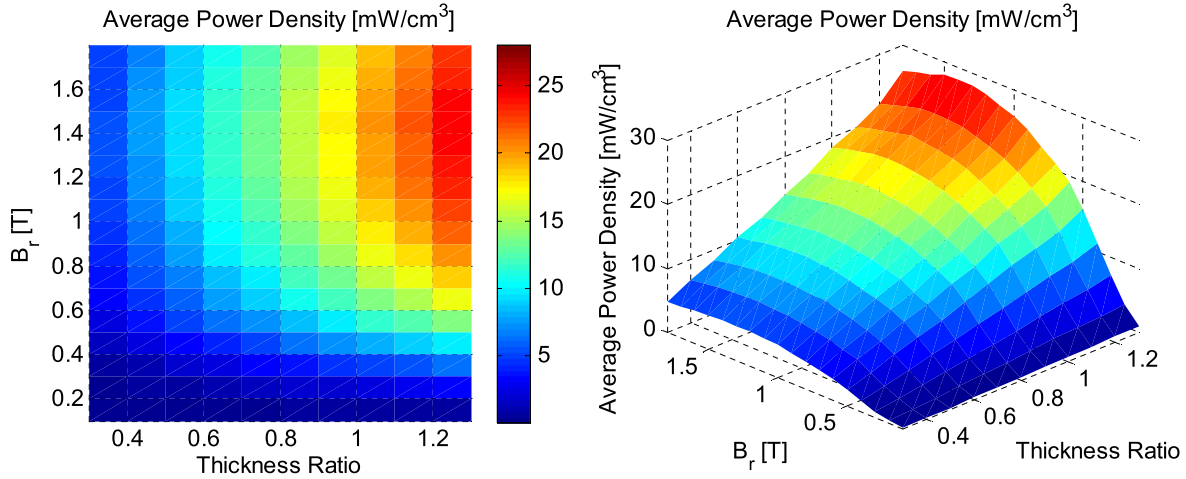


**Figure 24.** Maximum average output power density  $\bar{D}_{\max}$  with respect to thickness ratio and bias magnetic strength for 200 Hz,  $9.8 \text{ m s}^{-2}$  base excitation.

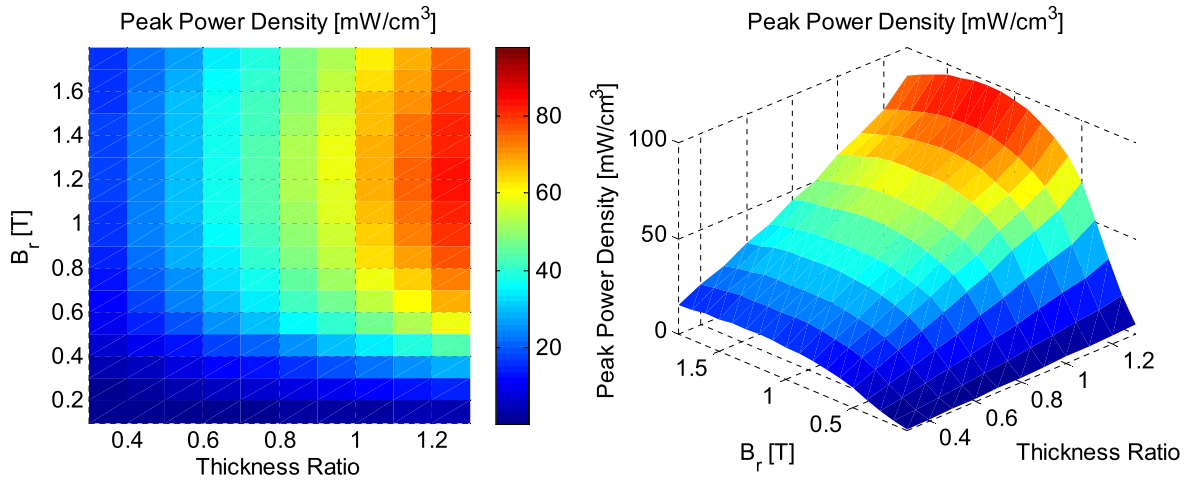


**Figure 25.** Maximum peak output power density  $Dp_{\max}$  with respect to thickness ratio and bias magnetic strength for 200 Hz,  $9.8 \text{ m s}^{-2}$  base excitation.

24, but the peak ( $Dp_{\max} = 97.6 \text{ mW cm}^{-3}$ ) is located in a different position (thickness ratio is 1.3 and  $B_r = 1.2 \text{ T}$ ).

#### 4. Summary and future work

This paper developed an efficient and accurate 2D FE model for Galfenol unimorph harvesters. Experimental results for 5 different unimorph beams demonstrate the accuracy of the model. The maximum average power density and peak power density measured from experiments are  $24.4 \text{ mW cm}^{-3}$  and  $63.6 \text{ mW cm}^{-3}$  by considering the Galfenol element surrounded by the pickup coil. A parametric study on the effect of pickup coil size, tip mass, thickness ratio, and bias magnetic field strength on harvester performance were presented. Optimal parameters targeting maximization of average output power was found for a 200 Hz,  $9.8 \text{ m s}^{-2}$  amplitude base vibration source. The optimal coil size was 800 turns using 36 AWG wire. The tip mass and thickness ratio relationship was found for a unimorph beam with a natural frequency of 200 Hz. The maximum average power and the maximum

average power density observed from modeling were  $1.0 \text{ mW}$  and  $28.1 \text{ mW cm}^{-3}$ , respectively, for a thickness ratio of 1.3 and a remanent flux density value of  $1.4 \text{ T}$ . The maximum peak power density achieved through modeling was  $97.6 \text{ mW cm}^{-3}$  when the thickness ratio was 1.3 and the remanent flux density produced by the bias magnet was  $1.2 \text{ T}$ .

Future studies may incorporate other physics into the optimization procedure such as the effect of different substrate materials, incidence of the glue layer on cantilever dynamics, more complex electrical circuitry, or dynamics of the excitation structure. However, doing so increases computational complexity beyond what is currently feasible for FE model-guided design. Ferrari *et al* [31] and Erturk *et al* [32] implemented strategies to improve the frequency bandwidth of a cantilever piezoelectric harvester, and similar approaches for Galfenol unimorph harvesters might be tested. Current experiments and simulations are limited to sinusoidal base excitations; research on improving the efficiency of harvesting energy from general vibration sources could be conducted following a study by Daqaq [33] that analyzed a



bistable system driven by white noise and exponentially correlated Gaussian noise.

## Acknowledgments

We wish to acknowledge the member organizations of the Smart Vehicle Concepts Center, a National Science Foundation Industry/University Cooperative Research Center ([www.SmartVehicleCenter.org](http://www.SmartVehicleCenter.org)) established under NSF Grant IIP-1238286.

## References

- [1] Clark A E, Wun-Fogle M, Restorff J B and Lograsso T A 2002 *Mater. Trans.* **43** 881–6
- [2] Restorff J, Wun-Fogle M, Clark A and Hathaway K 2006 *IEEE Trans. Magn.* **42** 3087–9
- [3] Wun-Fogle M, Restorff J and Clark A 2006 *IEEE Trans. Magn.* **42** 3120–2
- [4] Kellogg R, Flatau A, Clark A, Wun-Fogle M and Lograsso T 2002 *J. Appl. Phys.* **91** 7821–3
- [5] Meninger S, Mur-Miranda J O, Amirtharajah R, Chandrakasan A and Lang J H 2001 *IEEE Trans. Very Large Scale Integr. (VLSI) Syst.* **9** 64–76
- [6] Glynne-Jones P, Tudor M, Beeby S and White N 2004 *Sensors Actuators A* **110** 344–9
- [7] Xing X, Lou J, Yang G M, Obi O, Driscoll C and Sun N X 2009 *Appl. Phys. Lett.* **95** 134103
- [8] Beeby S P, Tudor M J and White N 2006 *Meas. Sci. Technol.* **17** R175
- [9] Roundy S, Wright P K and Rabaey J 2003 *Comput. Commun.* **26** 1131–44
- [10] Erturk A, Hoffmann J and Inman D 2009 *Appl. Phys. Lett.* **94** 254102
- [11] Wang L and Yuan F 2008 *Smart Mater. Struct.* **17** 045009
- [12] Berbyuk V 2013 *Proc. SPIE* **8688** 86881F
- [13] Yoo J H and Flatau A B 2012 *J. Intell. Mater. Syst. Struct.* **23** 647–54
- [14] Yoo J H, Flatau A and Purekar A 2011 *Proc. ASME* **1** 391–6
- [15] Ueno T and Yamada S 2011 *IEEE Trans. Magn.* **47** 2407–9
- [16] Chakrabarti S and Dapino M J 2011 *Smart Mater. Struct.* **20** 105034
- [17] Deng Z and Dapino M J 2015 *J. Intell. Mater. Syst. Struct.* **26** 47–55
- [18] Rezaeealam B, Ueno T and Yamada S 2012 *IEEE Trans. Magn.* **48** 3977–80
- [19] Armstrong W 2003 *J. Magn. Magn. Mater.* **263** 208–18
- [20] Evans P and Dapino M 2010 *J. Appl. Phys.* **107** 063906
- [21] Kittel C 1949 *Rev. Mod. Phys.* **21** 541
- [22] Shu L, Dapino M J, Evans P G, Chen D and Lu Q 2011 *J. Intell. Mater. Syst. Struct.* **22** 781–93
- [23] Shu L, Headings L M, Dapino M J, Chen D and Lu Q 2014 *J. Intell. Mater. Syst. Struct.* **25** 187–203
- [24] Kiral Z 2009 *J. Reinf. Plast. Compos.* **28** 2511–26
- [25] Clough R W and Penzien J 1993 *Dynamics of Structures* vol 634 (New York: McGraw-Hill)
- [26] Yoo J, Murray A and Flatau A 2014 *Proc. SPIE* **9057** 905731
- [27] Mitcheson P, Yeatman E, Rao G, Holmes A and Green T 2008 *Proc. IEEE* **96** 1457–86
- [28] Deng Z and Dapino M 2008 *Proc. SPIE* **9433** 94330B
- [29] Deng Z and Dapino M 2014 *Proc. SPIE* **9057** 90572A
- [30] Weng L, Walker T, Deng Z, Dapino M and Wang B 2013 *J. Appl. Phys.* **113** 024508
- [31] Ferrari M, Ferrari V, Guizzetti M, Andò B, Baglio S and Trigona C 2010 *Sensors Actuators A* **162** 425–31
- [32] Erturk A and Inman D 2011 *J. Sound Vib.* **330** 2339–53
- [33] Daqaq M F 2011 *J. Sound Vib.* **330** 2554–64